Atmos. Chem. Phys. Discuss., 12, 25441–25485, 2012
www.atmos-chem-phys-discuss.net/12/25441/2012/
doi:10.5194/acpd-12-25441-2012

Atmospheric Chemistry and Physics Discussions

The first aerosol indirect effect quantified through airborne remote sensing during VOCALS-REx

D. Painemal[1] **and P. Zuidema**[2]

[1]NASA Langley Research Center, Hampton, VA, USA
[2]Rosenstiel School of Marine and Atmospheric Sciences, University of Miami, Key Biscayne, FL, USA

Received: 5 September 2012 – Accepted: 8 September 2012 – Published: 25 September 2012

Correspondence to: D. Painemal (david.painemal@nasa.gov)

Published by Copernicus Publications on behalf of the European Geosciences Union.

Abstract

The first aerosol indirect effect (1AIE) is investigated using a combination of in situ and remotely-sensed aircraft (NCAR C-130) observations acquired during VOCALS-REx over the Southeast Pacific stratocumulus cloud regime. Satellite analyses have previously identified a high albedo susceptibitility to changes in cloud microphysics and aerosols over this region. The 1AIE was broken down into the product of two independently-estimated terms: the cloud aerosol interaction metric $\mathrm{ACI}_\tau = \frac{\mathrm{d}\ln\tau}{\mathrm{d}\ln N_\mathrm{a}}\Big|_\mathrm{LWP}$, and the relative albedo (A) susceptibility $S_{\mathrm{R}-\tau} = \frac{\mathrm{d}A}{3\mathrm{d}\ln\tau}\Big|_\mathrm{LWP}$, with τ and N_a denoting retrieved cloud optical thickness and in-situ aerosol concentration, respectively and calculated for fixed intervals of liquid water path (LWP). ACI_τ was estimated by combining in-situ N_a sampled below the cloud, with τ and LWP derived from, respectively, simultaneous upward-looking broadband irradiance and narrow field-of-view millimeter-wave radiometer measurements, collected at 1 Hz during four eight-hour daytime flights by the C-130 aircraft. ACI_τ values were typically large, close to the physical upper limit (0.33), increasing with LWP. The high ACI_τ values were in agreement with other in-situ airborne studies in pristine marine stratocumulus and reflect the imposition of a LWP constraint and simultaneity of aerosol and cloud measurements. $S_{\mathrm{R}-\tau}$ increased with LWP and τ, reached a maximum $S_{\mathrm{R}-\tau}(0.086)$ for LWP (τ) of 58 $\mathrm{g\,m^{-2}}$ (13–14), decreasing slightly thereafter. The net first aerosol indirect effect thus increased over the LWP range of 30–80 $\mathrm{g\,m^{-2}}$. These values were consistent with satellite estimates derived from instantaneous, collocated CERES albedo and MODIS-retrieved droplet number concentrations at 50 km resolution. The consistency of the airborne and satellite estimates (for airborne remotely sensed $N_\mathrm{d} < 1100\,\mathrm{cm^{-3}}$), despite their independent approaches, differences in observational scales, and retrieval assumptions, is hypothesized to reflect the robust remote sensing conditions for these homogeneous clouds. We recommend the Southeast Pacific for a regional assessment of the first aerosol indirect effect in climate models on this basis.

ACPD
12, 25441–25485, 2012

1 Introduction

The First Aerosol Indirect Effect (1AIE) is the cloud albedo enhancement that results from an increase in the cloud droplet number concentration and optical thickness due to increases in the aerosol burden with all other cloud properties, typically cloud liquid water path, held constant (Twomey, 1977). This effect has by now been widely observed. Large-scale model comparisons with selected observations (e.g., Quaas et al., 2009) reveal a large spread among the different 1AIE estimates. This suggests that further observational estimates of the first AIE for specific well-characterized regions can be valuable for assessing model behavior more deeply.

An adequate evaluation of 1AIE requires taking into account its two components, that is, the effect of the aerosols on the cloud microphysics (cloud-aerosol interactions), and the albedo perturbations that arise from the changes in the cloud properties. The aerosol-cloud interactions (ACI) component has typically been investigated with a simple metric proposed by Feingold et al. (2001):

$$\mathrm{ACI_N} = \left.\frac{\mathrm{d}\ln N_\mathrm{d}}{\mathrm{d}\ln N_\mathrm{a}}\right|_\mathrm{LWP} \tag{1}$$

N_a and N_d are the aerosol and the cloud droplet number concentration, respectively. One approach for isolating the aerosol effect from dynamical influences is to calculate $\mathrm{ACI_N}$ for constrained values of the cloud liquid water path (LWP). Alternatively, the metric can be also expressed in terms of the cloud optical thickness τ or cloud effective radius r_e as:

$$\mathrm{ACI}_\tau = \left.\frac{\partial\ln\tau}{\partial\ln N_\mathrm{a}}\right|_\mathrm{LWP} \qquad \mathrm{ACI_r} = \left.\frac{\partial\ln r_\mathrm{e}}{\partial\ln N_\mathrm{a}}\right|_\mathrm{LWP} \tag{2}$$ (McComiskey and Feingold, 2008)

When the cloud structure is well described by an adiabatic-like stratification of the water content, with a constant N_d with height, and r_e that linearly increases from the cloud base, the three different ACI can be related as:

$$\mathrm{ACI_N} = 3\cdot\mathrm{ACI}_\tau = -3\cdot\mathrm{ACI_r} \tag{3}$$

ACPD
12, 25441–25485, 2012

The coefficient 3 in the equality (3) arises from the relationships $N_d \propto LWP^{1/2} r_e^{-3}$ with $LWP \propto \tau \cdot r_e$ (Bennartz, 2007). If one assumes that a fractional change in N_a cannot produce a larger fractional change in N_d, then $ACI_N \leq 1$. Thus, according to (3): $ACI_\tau - ACI_r \leq 0.33$. In more complex environments like those found in heavily polluted continental areas, changes in cloud microphysics also depend on the shape of the aerosol size distributions, solubility and updrafts velocity, and the ACI metrics become less suitable estimators of the aerosol-cloud interactions. Nevertheless, these simple metrics should capture most of the aerosol influence in the cloud (Feingold, 2003), particularly for the relatively pristine marine air of the Southeast Pacific.

The component of 1AIE that links perturbations in the cloud microphysics with changes in albedo (A) can be expressed through the albedo susceptibility metric (S), defined as:

$$S = \left.\frac{dA}{dN_d}\right|_{LWP} \quad \text{(4) Platnick and Twomey (1994)}$$

Or, in terms of fractional changes of N_d, as the relative albedo susceptibility (S_R):

$$S = \left.\frac{dA}{d\ln N_d}\right|_{LWP} \quad \text{(5) Platnick and Oreopulos (2008)}$$

We can finally quantitatively reconstruct the 1AIE by combining ACI_N and S_R:

$$1AIE = \left.\frac{dA}{d\ln N_a}\right|_{LWP} = ACI_N \cdot S_R \quad (6)$$

In this investigation, we assess the first aerosol indirect effect for Southeast Pacific stratocumulus clouds. This marine region contains one of the most extended and persistent stratocumulus decks on the planet. Satellite analyses have revealed global-maximum values of the albedo susceptibility (S_R) component of the 1AIE for the Southeast Pacific (e.g. Oreopoulos and Platnick, 2008; Painemal and Minnis, 2012), in part because

ACPD
12, 25441–25485, 2012

a dry free troposphere does little to attenuate the top-of-cloud albedo (Zuidema et al., 2012; Painemal and Minnis, 2012). However, comprehensive ACI calculations have not yet been carried out to date for this region, and a quantification of the first aerosol indirect effect is lacking. The aerosol and cloud microphysics interactions component cannot be as easily explored with passive satellite observations. A serious issue is the impossibility of retrieving aerosols over cloudy scenes, so that cloud and aerosol retrievals are not spatially collocated. In situ and land (surface)-based observations are deemed to be more accurate, but different studies report a wide range of estimates of ACI (see McComiskey and Feingold, 2008, for a review). This apparent inconsistency has been explained by dissimilar spatial/temporal resolution of the observations, biases inherent to the retrievals, lack of LWP constraint, and potential regime-dependent differences (McComiskey and Feingold, 2012). We explore these issues for this region, using airborne in situ and remotely-sensed observations, and by comparing the airborne-derived numbers to satellite estimates.

We take advantage of the high temporal resolution observations collected by the NSF/NCAR aircraft C-130 during the VAMOS Ocean-Cloud-Atmosphere-Land System Regional Experiment (VOCALS-REx, Wood et al., 2011). Other airborne assessments of the first aerosol indirect effect have used microphysical data taken during aircraft soundings to compute vertically-integrated variables such as LWP and τ (e.g., Twohy et al., 2005). Such an analysis is also performed here using almost 100 daytime aircraft vertical profiles that were collected during VOCALS-REx. The unprecedented (to our knowledge) airborne remote sensing analysis within this study, however, is potentially capable of providing many more samples. Specifically, we combined daytime aerosol concentration measurements sampled within the marine boundary layer during 10-min subcloud legs, with simultaneous aircraft remotely-sensed LWP and τ. The algorithm for retrieving LWP from an airborne millimeter-wave radiometer is documented in Zuidema et al. (2012). The physical algorithm for estimating τ from combining shortwave irradiances measured by an hemispheric Eppley Precision Spectral Pyranometer combined with a plane-parallel radiative transfer model, is presented here.

ACPD
12, 25441–25485, 2012

2 Dataset

Upward-looking airborne radiometers sampled continuously during sub-cloud transects (150–200 m above the sea level), with a hemispheric field-of-view for the broadband shortwave measurements. The 1.7 degree beam width of the millimeter-wavelength radiometer corresponds to an ∼ 30 m horizontal spatial resolution for a typical 500 m aircraft-to-cloud distance. In contrast, the broadband irradiance measurements sample a horizontal area of 860 m (1375 m) within a viewing angle measured from nadir of 60° (70°). The sub-cloud aerosol concentration measurements were collected simultaneously by a Passivity Cavity Aerosol Probe (PCASP). Since the τ retrievals were based on solar transmission calculations, our analysis was limited to daytime flights (when the 1AIE is important). We selected four from a total of six daytime flights performed by the aircraft C-130, with an approximate duration of 8 h and 1 Hz sampling (Table 1). The two excluded flights either did not sample much cloud, and/or encountered frequent precipitation, both of which are unfavorable for retrieving LWP and τ and do not consist physical realms in which the first aerosol indirect effect applies.

2.1 Regional context

Figure 1 depicts the regional maps of satellite-based N_d and LWP from MODIS-Terra (∼ 10:30 local time) for the four daytime flights and their respective aircraft trajectories. RF02 (18 Otcober) had the largest N_d, with typical values higher than 300 cm^{-3}, indicative of a significant aerosol impact in the cloud properties. For RF01 (15 October), RF11 (9 November), and RF12 (11 November), the high N_d plume covered a smaller area, and was mainly confined to the coast, with the smallest extension during RF11. 18 October (RF02) was a member of the 6-yr high-N_d tercile group examined within Painemal and Zuidema (2010). High-N_d days were on average more stable near the coast, with thinner clouds, than low-N_d days (Painemal and Zuidema, 2010). Overall, the satellite N_d maps anticipate aircraft sampling of a wide range of aerosol loadings under the same meteorology, which is desired for investigating the first indirect effect.

ACPD
12, 25441–25485, 2012

RF01, RF11 and RF12 favored the sampling of coastal regions that were more prone to anthropogenic influences, whereas the westward sampling in RF02 sampled offshore clouds that were characterized by a deeper boundary layer, and lower aerosol concentration than near the coast (e.g. Painemal and Zuidema, 2010; Allen et al., 2011; Bretherton et al., 2010).

The surface meteorological pattern (Fig. 2), as expected, is described by a persistent anticyclone and surface winds parallel to the coast with calmer winds within the Arica Bight (20° S, 72° W). More interesting is the case-to-case variability in winds associated with a coastal jet (Munoz and Garreaud, 2005). For a high-N_d day such as 18 October (RF02), the anticyclone and coastal winds are weaker and boundary layer shallower, than for a day with lower N_d such as 9 November (RF11) (Painemal and Zuidema, 2010; Zheng et al., 2011).

2.2 Liquid water path (LWP)

An airborne G-band (183 GHz) vapor radiometer (GVR), with an upward pointing orientation, was utilized to retrieve LWP. The GVR, designed by ProSensing Inc., measures radiances from double sideband channels at ±1, ±3, ±7 and ±14 GHz from the 183.31 GHz line (Pazmany et al., 2006). The wing-line ±14 GHz band is best suited for retrieving liquid water because of its higher sensitivity to liquid water. The above-aircraft water vapor path was sufficient to saturate the center absorption lines, and independent estimates of water vapor were prescribed to isolate the liquid water absorption signal. The water vapor path (WVP) within the flight level and the cloud base was estimated from aircraft measurements of water vapor mixing ratio, assuming that the total moisture was conserved up to the lifting condensation level, with an additional adjustment when the boundary layer was decoupled (Zuidema et al., 2012). The in-cloud water vapor was adiabatically calculated. Additionally, the free tropospheric water vapor path was retrieved from the GVR during above-cloud flight legs (free tropospheric WVP did not saturate the absorption lines), and then summed with the boundary-layer WVP to produce the total WVP. The retrieval algorithm iterated between a model-calculated

ACPD
12, 25441–25485, 2012

brightness temperature and the observed brightness temperature (±14 GHz band) to find the LWP providing the closest brightness temperature match (Zuidema et al., 2012). Comparisons of GVR LWP against its adiabatic counterpart showed good correlations and statistically smaller GVR LWP, which is consistent with an expected but small cloud sub-adiabaticity (Zuidema et al., 2012). A conservative absolute error in the leg-mean LWP was estimated at 20 g m^{-2}, with larger uncertainties for precipitating clouds and decoupled boundary layers.

2.3 Cloud optical thickness (τ)

The pyranometer-based τ retrieval relied on the strong dependence of τ on the incoming solar radiation and the solar zenith angle, with secondary dependences on r_e and the atmospheric composition (Leontyeva and Stamnes, 1994). The algorithm consisted of iterative radiative transfer simulations targeted to find the optimal τ that matched the pyranometer irradiance. The forward calculations of irradiance were performed with Streamer model (Key and Schweiger, 1998); a versatile DISORT-based radiative transfer model that has been successfully applied to the study of Arctic stratus clouds (e.g. Pinto, 1997; Zuidema et al., 2005). The model employs the Hu and Stamnes (1993) parameterization to calculate the single scattering albedo, volume extinction coefficient, and asymmetry factor from a specified cloud effective radius. The Streamer simulations applied to the spectral band 0.28 µm–2.91 µm, which is slightly broader than the spectral band measured by the pyranometer (0.28 µm–2.8 µm). This spectral difference was independently examined with the higher-spectral-resolution SBDART model (Richiazzi et al., 1998) and found to be an insignificant source of error (less than 1 W m^{-2}). The solar zenith angle was calculated from the flight UTC time and the aircraft spatial coordinates.

ACPD
12, 25441–25485, 2012

2.3.1 Model-pyranometer bias

We first tested the model performance against in-situ pyranometer clear-sky observations. We focused on 11 November flight (RF12) measurements collected ∼ 200 m above the sea level (sub-cloud). Two periods with extended clear sky conditions, as determined by the Wyoming cloud lidar, were utilized for the initial assessment. We prescribed the WVP as in Zuidema et al. (2012), and assumed an aerosol optical thickness of 0.05 and a standard McClatchey summer midlatitude profile of atmospheric gases (Fig. 3, red line, standard simulation). The simulated irradiances in Fig. 3a (red line) underestimated the pyranometer observations (black line), especially during the first period (mean bias of 80 $W m^{-2}$), but with a reduction later on (20 $W m^{-2}$) at a lower zenith angle.

The rather unexpected model bias was further analyzed by determining the sensitivity of the simulated fluxes to the atmospheric composition. Three additional simulations included cases with 50 % reduction in WVP, pristine conditions without aerosols, and negligible absorbing gases (ozone and tracing gases) (Fig. 3a, blue line, green triangles, and magenta circles, respectively). While reductions in any atmospheric quantity produced larger shortwave fluxes, these changes could not explain why the model underestimated the observed irradiance.

Given the scarcity of clear-sky observations, we carried out a more systematic analysis of the pyranometer-model bias using above-clouds measurements and simulated irradiances for the four research flights considered in this investigation. We prescribed a mean free tropospheric water vapor path of 3 mm, standard values of atmospheric gases for a summer mid-latitude atmosphere, and a fixed aerosol optical thickness at 0.05. Figure 3b shows the relationship between simulated and observed fluxes at heights between 1400–1700 above the sea level. Although both fluxes correlated well, the simulated ones were lower, with a bias that increased with Q, as it was anticipated in Fig. 3a.

ACPD
12, 25441–25485, 2012

The persistent negative offset in our simulations was not consistent with an aircraft attitude (pitch/roll) effect, since that would produce both anomalous high and low pyranometer irradiances relative to observations collected over a fixed horizontal plane. We suspected potential pyranometer calibration errors that could not be verified, as we did not count on assessments of the pyranometer performance prior and after the flights. Nevertheless, calibration problems were plausible as previous airborne field experiments noted systematic instrument offsets (e.g. Kato et al., 1997; Bush et al., 2000). For instance, comparison of five uncalibrated Eppley pyranometers during the Atmospheric Radiation Measurements Enhanced Shortwave Experiment (ARESE) revealed irradiance differences of up to 5 % (Kato et al., 1997).

Since the inconsistency between modeled and measured irradiance might severely affect the cloud optical thickness retrievals, we adjusted the pyranometer irradiance ($Q_{\text{pyr-adj}}$) through a linear regression that fitted above-clouds pyranometer fluxes with the simulated clear-sky irradiances (Eq. 7).

$$Q_{\text{pyr-adj}} = a \cdot Q_{\text{pyr}} + b \tag{7}$$

Q_{pyr} indicates the measured pyranometer irradiance. Typically the slope a encompasses values between 0.9 and 0.97 (Table 2). This adjustment proved to significantly reduce the bias in Fig. 3a to amounts smaller than 10 W m^{-2}. Hereafter, we only make use of the adjusted pyranometer irradiance (denoted as Q_{pyr}).

2.3.2 Retrieval algorithm

Inputs for the retrieval algorithm included the WVP as described in Sect. 2.3.1, constant aerosol optical thickness of 0.05, and McClatchey mid-latitude summer profiles for the ozone and trace gases (Key and Schweiger, 1998). The simulations were further simplified by assuming a vertically homogeneous cloud with a constant r_e with height.

In the first stage of the algorithm, we prescribe initial τ (τ^*) and r_e (r_e^*) and perform 2-streams simulations to estimate the irradiance $Q(r_e^*, \tau^*)$. The initial r_e^* and τ^* were adiabatically calculated from GVR LWP and a simple empirical N_d proxy expressed as

ACPD
12, 25441–25485, 2012

$N_d = 50 + 0.5 \times N_a$ (Jeff Snider, 2012, personal communication). If the absolute value $|Q(r_e^*, \tau^*) - Q_{pyr}| > 3\,W\,m^{-2}$, then τ^* is increased (decreased) by 0.04 when $Q(r_e^*, \tau^*)$ is larger (smaller) than Q_{pyr}, and the irradiance is calculated again with the prescribed r_e^*. When $|Q(r_e^*, \tau^*) - Q_{pyr}| < 3\,W\,m^{-2}$ the iteration ends and r_e^* is upgraded to $r_e^* = \frac{9}{5\tau^*} \times LWP$ (Bennartz, 2007), and the retrieved τ^* and r_e^* are used for the next loop.

A second two-streams loop, identical to the previous one, is made with the upgraded r_e^* and τ^*. r_e^* is upgraded for the last time at the end of the loop, and the pair $r_e^* - \tau^*$ is used for the next and final iteration. For the final loop, we expanded the number of discrete ordinates to eight streams, and continued the simulations until the simulated fluxes differ in $3\,W\,m^{-2}$ from the observed fluxes.

2.3.3 τ uncertainties

We explore the impact of the following uncertainties in τ: vertically homogeneous cloud assumption, errors in water and liquid water path, and errors in the pyranometer observations. The effect of assuming a constant water content and r_e with height is assessed by retrieving τ using synthetic irradiances calculated for a cloud with an adiabatic vertical stratification. We find a small τ bias, with τ exceeding its adiabatic counterpart by 0.2, consistent with a lack of sensitivity to the vertical profile described in Brenguier et al. (2000) but for narrow band measurements. A ±30 % error in the specified WVP would produce typical τ bias smaller than 4 %, in agreement with Leontyeva and Stamnes (1994). In addition, we also analyze the effect of uncertainties in LWP error by assuming 30 % variations (equivalent to 30 % variations in r_e). We find that the mean error in τ is close to 5 %, with a negative (positive) bias when LWP is biased low (high).

We finally explore the effect of the pyranometer uncertainties in the retrieved τ. We assume a conservative error of 5 % in the pyranometer signal, a value that accounts for the mean error that could arise from the mismatch between observations and the radiative model found in Sect. 2.3.1. After applying the retrieval algorithm to the modified pyranometer fluxes, we found biases between 15 % ($\Delta\tau = 0.6$) and 5 % ($\Delta\tau = 2$)

ACPD
12, 25441–25485, 2012

for a range of τ between 4 and 40, respectively (Fig. 4). Based on these results, we estimate a conservative mean τ uncertainty near 10 %.

2.4 LWP-τ consistency and general overview

Figure 5 shows a ten minutes time series during RF02 of the variables used to compute the ACI: GVR LWP and τ (Fig. 5a), N_d (Fig. 5b, Eq. 8) and N_a (Fig. 5c). The near 10 min sampling in Fig. 5 is equivalent to a 60 km transect (mean aircraft speed of 100 m s^{-1}), which would explain the apparent high variability in the time series. LWP and τ show the expected correlation (Sect. 2.4), but with a less variable τ. This is because the pyranometer collects hemispheric incident solar radiation, and therefore, the retrieved τ is an effective measurement representative of a broad ($\sim$ 1 km) cloudy area. In general, spatial/temporal changes in τ attributed to N_a are difficult to observe because of the boundary layer control in the evolution of the cloud properties. This further stresses the importance of investigating the τ-N_a interactions within a constant dynamical configuration or LWP.

We determined the physical consistency of the remotely sensed LWP-τ pairs through comparisons to their in situ counterparts. Since the GVR LWP estimate was less accurate in decoupled boundary layers, we eliminated samples with lidar-based cloud base height and lifting condensation level differences larger than 150 m (Jones et al., 2011). We reduced the effect of broken clouds in the pyranometer field of view by removing samples that did not occur 7 s prior and after cloudy observations (1.4 km cloudy horizontal transect). In addition, drizzling cases were excluded using a radar reflectivity threshold of −17 dBZ. After applying the aforementioned screening, we availed ourselves of 4490 samples, with 80 % of them collected during RF02 and RF12. Figure 6a depicts the relationship between τ and LWP for both remote-sensing and in-situ variables during the four daytime flights (black dots and red circles, respectively). In-situ and remote sensing observations showed a high LWP-τ correlation with an agreement in the slope, indicating the physical consistency of the retrievals.

ACPD
12, 25441–25485, 2012

We carried out an additional indirect retrieval assessment by comparing a histogram of in-situ N_d to an adiabatic-like N_d, derived from the remote sensing observations as follows:

$$N_d = 0.05789\,[\mathrm{g^2\,cm^{-6}}] \cdot \frac{\Gamma^{1/2}}{k} \cdot \frac{\tau^3}{\mathrm{LWP}^{5/2}} \quad (8)$$

where Γ is the local stratification of the water content with height, and k is the ratio between the cube of the effective radius and the volume radius of the droplet size distribution. This N_d is similar to the one applied within Painemal and Zuidema (2011) to MODIS data, but cast in terms of LWP and a non-constant Γ. Γ corresponded to the adiabatic lapse rate, calculated every second from remote-sensed cloud base height and temperature, and multiplied by 0.7, a factor that accounted for the sub-adiabaticity of the clouds. For k, we selected a constant mean value of 0.88 at the cloud top derived from the aircraft cloud probes. Qualitatively, the N_d histograms (Fig. 6b) agreed relatively well, with a mode near 200 $\mathrm{cm^{-3}}$. Nevertheless, the remotely-sensed airborne N_d had more cases with concentrations larger than 450 $\mathrm{cm^{-3}}$, values rarely observed by the C-130 cloud probes. This could imply a LWP underestimate or a cloud optical depth underestimates. Differences in the instruments field of view, manifested in a higher temporal variability in LWP, are also a factor to take into account. For instance, we observed in Fig. 5 that local minima in LWP led to a sharp increase in N_d (Fig. 5b). The time series also indicated that some cases with high N_d were associated with small LWP ($< 20\,\mathrm{g\,m^{-2}}$, Fig. 5b, 17:30–17:33 UTC). The influence of high N_d in our results will be discussed in Sects. 3 and 4.

The agreement between the modes of the in-situ and retrieved N_ds histograms in Fig. 6b suggest then a high degree of spatial homogeneity within the stratocumulus deck. This is also evident within a heterogeneity index (H_σ) calculated as the ratio of the standard deviation to the mean LWP for a 11 s moving window (1.1 km). This definition is similar to a previously-used satellite-derived H_σ that was spatially calculated from the 0.86 µm MODIS visible reflectance (e.g. Zhang and Platnick, 2011; Di Girolamo

ACPD
12, 25441–25485, 2012

et al., 2010). The H_σ calculated here encompassed values between 0–1 (consistent with satellite estimates), with a mean H_σ of 0.2 and a standard deviation of 0.15. These values are approximately similar to those reported by Cahalan et al. (1994) based on 18 days of microwave LWP data from Californian stratus. Zhang and Platnick (2011) found evidence of 3-D effects in MODIS retrievals for MODIS-based H_σ values larger than 0.3. If our LWP-based results can be approximately compared to the satellite-based $H\sigma$, the LWP-based H_σ values do suggest that the clouds investigated here were mostly homogeneous. Lastly, we note that our samples were associated with solar zenith angles between 10 and 50°. For the observations collected near-nadir, three-dimensional photon leakage may also contribute to a retrieved cloud optical depth and N_d underestimate. We emphasize that the retrieved N_d do not contribute to the calculation of ACI_τ or S_R. We do, however, analyze the ACI_τ dependence on N_d, using N_d to indicate the level of physical agreement of the τ-LWP pair.

With available estimates of τ and LWP, simultaneous PCASP aerosol observations completed the set of variables needed to calculate ACI_τ. Although the University of Wyoming cloud condensation nuclei (CCN) counter operated during sub-cloud transects, the measurements had a relatively low temporal resolution (20 s) and did not operate during one of the flights. The variables and dependences used in this investigation are listed in Table 3. The probability density functions for LWP, τ, and N_a for the four selected flights are depicted in Fig. 7. Mode values for LWP, τ, and, N_a are 45 g m^{-2}, 8, and 230 cm^{-3}, respectively. Mean LWP and τ (50 g m^{-2} and 12.6) are fairly consistent with a satellite climatology that shows the largest (smallest) τ (LWP) along the Chile coast (Painemal and Minnis, 2012).

3 Results

The relationship between τ and N_a, for the four flights, and irrespective of LWP, is depicted in Fig. 8. As expected, we found a positive correlation (r = 0.59) with magnitudes for N_a within 70–800 cm^{-3}. The absence of smaller N_a was explained by the removal

ACPD
12, 25441–25485, 2012

of drizzling samples (> −17 dBZ) in our dataset. While the high correlation does show a link between aerosol concentration and cloud optical properties, the next step is to isolate the aerosol impact from the effect of the cloud macrophysical properties. This was done by imposing a LWP binning.

3.1 ACI calculations

Since τ, LWP, and N_a, were derived independently of each other, we adopted ACI_τ to investigate 1AIE. Our simple approach was to compute ACI_τ for different LWP intervals, and calculate the slope between $\ln(N_a)$ and $\ln(\tau)$ (McComiskey et al., 2009). In addition to the screening detailed in Sect. 2.4, we only considered samples with $\tau > 2$, to reduce the measurements more prone to retrievals artifacts. We performed the regressions using an iterative reweighted least square fit, with a bi-square weighting function (Street et al., 1988), to reduce the effect of outliers.

Figure 9 illustrates ACI_τ differences between two LWP partitions. For both bins, ACI_τ reached or slightly surpassed the upper physical bound (0.33 and 0.34 for 70–80 g m^{-2} bin, and 50–60 g m^{-2} bins, respectively). The ACI dependence on LWP was more systematically evaluated by calculating ACI_τ for a set of LWP bins defined as:

$$\mathrm{Bin}_i = [0.9 \cdot \mathrm{LWP}_i \quad 1.1 \cdot \mathrm{LWP}_i]$$
$$\mathrm{LWP}_i = 30, 31, ..., 80\,\mathrm{g\,m^{-2}} \tag{9}$$

The relationship in Eq. (9) is equivalent to defining a bin width 20 % the size of the geometrical center of the bin LWP_i. This bins width was selected because it yielded a relatively similar number of samples among bins. Although only five bins did not overlap each other (e.g. 30, 37, 45, 55, and 68 g m^{-2} bins), we also calculated ACI_τ by shifting the bin center every 1 g m^{-2} (Eq. 9), in order to show the transition of ACI_τ with more continuous variations in LWP, and explore the robustness of the calculation for any given LWP_i. In addition, the sensitivity of ACI_τ to N_d was studied by removing samples linked to N_d larger than some arbitrary thresholds.

ACPD
12, 25441–25485, 2012

Figure 10 illustrates the dependence of ACI_τ on LWP and N_d, with slopes and correlation statistically significant at the 99.9 % confidence level according to a one tailed Student's t-test. For high N_d thresholds ACI_τ fluctuated between 0.26–0.4, with larger values for LWP near 60–67 $g\,m^{-2}$, an interval that also possessed the largest correlation and number of samples (0.7, black contours; and 500, magenta contours, respectively). The removal of samples with N_d larger than 1100 cm^{-3} mainly affected the smaller LWPs, because large N_d mostly occurred in those LWP bins. A further reduction in N_d produced ACI_τ that increased with LWP, with values closely bounded by the upper physical limit (0.33). More stringent N_d thresholds ($N_d < 600\,cm^{-3}$) reduced the Na-τ correlation, yielded a mean $ACI_\tau < 0.2$, whereas the slopes became statistically insignificant when LWP < 55 $g\,m^{-2}$. The ACI_τ-LWP dependence was relatively insensitive to the selected bin size, with a bin widening producing a modest increase in ACI_τ (not shown).

We further repeated the previous analysis but applying a 15-s moving average to LWP ($\overline{LWP}_{15s}$) and N_a (~ 1.5 km equivalent scale). ACI_τ maps obtained with $\overline{LWP}_{15s}$ and averaged N_a are depicted in Fig. 11. The overall N_a-τ correlation and number of samples increased in Fig. 11 relative to the native resolution counterpart (Fig. 10). The dependences of ACI_τ on LWP and N_d is more clearly depicted in Fig. 12 for four different cases: ACI_τ estimated irrespective of N_d (gray lines), and ACI_τ for $N_d < 1100$, 900, and 700 cm^{-3} (black, red, and blue lines, respectively). Dashed lines are the estimates derived with $\overline{LWP}_{15s}$. As in Fig. 10, Fig. 12 shows that ACI_τ increased with LWP, and with N_d. ACI_τ calculated with $\overline{LWP}_{15s}$ (Fig. 12, dashed lines) yielded less smooth transitions with liquid water path, and larger magnitudes especially for $N_d < 900$ and 700 cm^{-3}.

The remote-sensing-based magnitudes of ACI_τ were compared against that derived from the aerosol and cloud probe measurements. Since the aerosol probe PCASP was not suited for in-cloud aerosol sampling, we used below cloud measurement instead. We averaged 30 s PCASP aerosol concentration immediately before (ascent profiles)

ACPD
12, 25441–25485, 2012

or after (descent profiles) the aircraft profile occurrence, and correlated them with the in-cloud profiles averaged N_d. In addition, samples with precipitating LWP (from the two dimensional cloud probe) higher than $5\,g\,m^{-2}$, LWP $< 10\,g\,m^{-2}$, and $N_d < 10\,cm^{-3}$ were discarded from the analysis. This was done to exclude drizzling and potentially broken clouds that might mask the aerosol indirect effect. ACI_N for a total of 70 samples was 0.76, with a linear correlation of 0.81 (Fig. 13), or an equivalent ACI_τ value of 0.25 ($ACI_N/3$). Moreover, ACI_N ($ACI\tau$) increased to 0.85 (0.28) for cases with LWP smaller than $40\,g\,m^{-2}$. This in-situ ACI_N was within the lower end of the range of the remote-sensing ACI_τ (averages between 0.25–0.32) and supported the idea of a large ACI occurrence for this marine stratocumulus cloud regime. Our results differ from those in Terai et al (2012), who reported an in situ ACI_N of 0.55. This discrepancy may be because Terai et al. (2012) relied on a larger dataset with more off-shore samples and included precipitating clouds. Moreover, their computation of ACI_N was obtained by maximizing the correlation between N_d and $N_a^{ACI_N}$. The estimate reported here is in better agreement with an independent aircraft-based study at 20° S and 72° W that reported $ACI_N = 0.71$ based on data collected in similar coastal daytime conditions (Zheng et al., 2011).

3.2 Albedo susceptibility and 1AIE

The link between changes in cloud microphysics and actual changes in the albedo was investigated by means of the albedo relative susceptibility metric (S_R). Because we intended to keep our analysis independently of a remotely sensed value of N_d, we used an alternative definition of S_R from Eq. (5) that was expressed in terms of τ, and accounts for most of the S_R magnitude (Platnick and Oreopoulos, 2008):

$$S_{R-\tau} = \frac{1}{3}\frac{dA}{d\ln\tau} \tag{10}$$

Albedo A was derived from Streamer plane-parallel 8-stream radiative simulations at the top of the atmosphere by using r_e and τ obtained from the iterative method in

ACPD
12, 25441–25485, 2012

Sect. 2.3. The high correlation between ln(τ) and A($r > 0.8$) simplified the ln(τ)–A slope calculation (Painemal and Minnis, 2012). Because the relative susceptibility calculation is sensitive to the solar zenith angle, we limited our analysis to samples with solar zenith angle within 15°–35°, an interval that allowed us to reduce S_R's range of variability (Platnick and Oreopoulos 2008). The solar zenith angle range selected was also in agreement with MODIS Terra pass over the region (e.g. Painemal and Minnis, 2012).

Similar to ACI$_\tau$, we computed $S_{R-\tau}$ for each LWP bin, using the same screening as in Sect. 2.4. $S_{R-\tau}$ typically increased with LWP and τ, reaching a maximum $S_{R-\tau}$ of 0.086 for LWP of 60 g m^{-2} and τ of 13–15, depending on the N_d threshold, and decreases thereafter (Fig. 14). It was also found that $S_{R-\tau}$ was relatively insensitive to the N_d threshold for LWP > 60 g m^{-2}, with a minimum of 0.082 for LWP (τ) of 80 (18). This result was surprisingly consistent with satellite estimations obtained by combining Cloud and the Earth's Radiant Energy System (CERES) albedo and Moderate Resolution Imaging Spectroradiometer (MODIS) cloud observations aboard Terra (10:30 local time pass), and over the same study region. Satellite estimates yielded $S_R = 0.083$, for LWP (τ) of 60 g m^{-2} (13–14) for coastal clouds, with a τ dependence consistent with two-streams expectations (Fig. 14, black dashed line). Both satellite and VOCALS susceptibilities were in qualitative agreement with the two-stream S_R (Twomey and Platnick, 1994) which increased with τ until reaching a maximum for τ of 13.33.

Relative susceptibilities for LWP < 60 g m^{-2} differed among different N_d cases. The largest $S_{R-\tau}$ corresponded to the calculation that used all the available samples, with magnitudes between 0.082–0.086 (Fig. 14, gray lines). In contrast, decreases in N_d yielded $S_{R-\tau}$ reductions to 0.76–0.78 for the smallest bins and a nearly monotonic increase with LWP until reaching their maxima $S_{R-\tau}$ for LWP at 60 g m^{-2}, as previously mentioned. Additionally, the cases with N_d constraints were in a closer agreement with satellite estimates. Samples with N_d < 700 cm^{-3} had the overall smallest $S_{R-\tau}$.

We note that $S_{R-\tau}$ and ACI$_\tau$ showed different functional dependences on LWP, with maximum $S_{R-\tau}$ co-occurring with a minimum ACI$_\tau$. This indicates that clouds that less efficiently change their cloud microphysics, due to changes in aerosols, can still

ACPD
12, 25441–25485, 2012

produce large changes in albedo, because of the radiative contribution of LWP. The dissimilar cloud radiative and microphysical response was more explicitly addressed, by combining ACI_τ and $S_{R-\tau}$ into the 1AIE metric. We calculated 1AIE as defined in Eq. (6), but using the conversion $ACI_N = 3ACI_\tau$ to relate ACI_τ and S_R:

$$1AIE = \left.\frac{d\ln A}{d\ln N_a}\right|_{LWP} = 3 \cdot ACI_\tau \cdot S_{R-\tau} \quad (11)$$

1AIE was only calculated for N_d thresholds smaller than $1100\,cm^{-3}$, because they produced more physically consistent ACI_τ. 1AIE, depicted in Fig. 15, showed minimum values for low LWP, mainly due to the influence of $S_{R-\tau}$. Similarly, large $S_{R-\tau}$ for LWP $> 68\,g\,m^{-2}$, produced a 1AIE maximum at 0.09 ($N_d < 900\,cm^{-3}$), or equivalent to an absolute change in albedo of 0.009 if N_a increased in 10 %.

A simple calculation can help to put in context the quantities derived in our study. If one assumes a typical daily mean incoming solar radiation at the top of the atmosphere of $400\,W\,m^{-2}$ (Petty, 2006), then a modest 10 % increase in N_a for LWP of $56\,g\,m^{-2}$ would produce a radiative forcing of approximately -2.3 to $-3.2\,W\,m^{-2}$ ($700\,cm^{-3} < N_d < 1100\,cm^{-3}$). These magnitudes are larger than the range derived from general circulation models (-1.8 to $-0.3\,W\,m^{-2}$, Quaas et al., 2009). The radiative forcing estimate is specific to this region and provides a test for climate model AIE estimates for Southeast Pacific stratocumulus.

4 Discussion

The higher ACI_τ values obtained with higher N_d thresholds are consistent with expectations for scale aggregation developed within McComiskey and Feingold (2012; MF12). High, physically-unrealistic N_d are more likely for more inhomogeneous scenes, for which the variability in LWP is inconsistent with the radiatively smoothed optical depth. The effects of this smoothing inherent to the cloud optical depth retrieval, and of the

ACPD
12, 25441–25485, 2012

additional LWP smoothing ($\overline{\text{LWP}}_{15s}$), is to reduce the variance within the dataset, increasing the correlation between optical depth–aerosol pairs. The ACI_τ increase when the samples were binned by their $\overline{\text{LWP}}_{15s}$ (Fig. 12, dashed lines), can be understood by considering that some τ that initially produced high N_d for periods of inhomogeneous LWP (e.g. Fig. 5), were unaffected by the N_d screening when this was calculated with $\overline{\text{LWP}}_{15s}$ (due to a reduction in N_d). This would imply that those τ that only passed the $\overline{\text{LWP}}_{15s}$-based N_d screening were more likely affected by cloud inhomogeneities. Thus, potential biases in τ due to 3-D radiative transfer effect could have an impact in the $\overline{\text{LWP}}_{15s}$-based ACI_τ. Addressing this problem is beyond the scope of this study, and will likely be investigated in a future work.

While our analysis suggests the usefulness of a N_d threshold to constrain different source of errors, this also raises the question of which threshold is most appropriate. Using the retrieved N_d values as a proxy for the aggregation of more inhomogeneous cloud properties, the arguments presented within MF12 would suggest the lower N_d threshold is more appropriate, because a reduction in cloud heterogeneity is apparent. We note that if we assume a maximum tolerable error in LWP and τ of 25 %, then the associated Gaussian propagation uncertainty in N_d is 98 %. That is to say, for a plausible theoretical maximum N_d of 450 cm^{-3}, the maximum retrieved N_d plus uncertainty would be as large as 891 cm^{-3}, equivalent to the 900 cm^{-3} threshold applied in this investigation.

This study's mean ACI value of 0.26–0.28 ($N_d < 900\,\text{cm}^{-3}$) was within the range, if near the higher end, of other in situ aircraft observations in marine stratocumulus that did not stratify for LWP (0.11–0.27, Table 1 in McComiskey and Feingold, 2008). A similar analysis using surface-based remotely-sensed variables at Pt. Reyes finds slightly smaller ACI values of 0.18–0.22 for the same range of LWPs compared to our estimates. We hypothesize that the higher ACI values reported here for the Southeast Pacific stratocumulus reflect in part the clouds high adiabaticity (Zuidema et al., 2012), for which the first aerosol indirect effect is optimized (Kim et al., 2008).

ACPD
12, 25441–25485, 2012

We found an increase of ACI_τ with LWP, while other studies have found an opposite trend but for a LWP range within 50 and 150 g m^{-2} (Kim et al., 2008; McComiskey et al., 2009). Collision/coalescence processes might modulate the dependence of ACI_τ on LWP, but this seems less likely for our samples given a mean LWP lower than 80 g m^{-2} and lack of precipitation (radar reflectivities were all < -17 dBZ). For instance, a simple calculation of coalescence loss rate for a cloud with a radar reflectivity of -17 dBZ or drizzle rate 0.1 mm day^{-1} (Comstock et al., 2004), and N_d of 200 cm^{-3}, yielded a modest 0.6 droplets/cc/hour loss rate (14.4 droplets/cc/day), according to the parameterization of Wood (2006). Thus, we hypothesize that the clouds studied here were mainly dominated by droplets condensational growth. For more sub-adiabatic clouds, cloud evaporation might reduce τ, counteracting the τ enhancement due to an increase in the aerosol concentration. The question that remains is whether the increase of ACI_τ with LWP found here reflects an actual aerosol activation enhancement. The results of an adiabatic parcel model shown in MF12 Fig. 11 also show an increase of ACI with LWP. We speculate, however, that this likely reflects LWP and ACI increases with vertical velocity, upon which aerosol activation depends. Within our dataset we found a decrease in the wind speed with increasing LWP. This may reflect the influence of the coastal jet; LWPs near the jet core, collected during RF11 and RF12, will be reduced (see Figs. 1 and 2) because enhanced mesoscale subsidence suppresses the boundary layer. The wind shear is also enhanced within the jet core (Munoz and Garreaud, 2005). The different near-coastal dynamical interactions may act to discourage aerosol activation and coincide with the lower LWPs, but this remains a speculation, that could not be explored further given the limitations of our dataset.

5 Concluding remarks

In this study, we combined remote sensing techniques to investigate the microphysical and radiative aspects of the first aerosol indirect effect. A strength of this study was the imposition of LWP constraints, and the availability of collocated aerosol-cloud property

ACPD
12, 25441–25485, 2012

measurements by virtue of the sub-cloud transects and remote sensing. The reliance on airborne remotely-sensed variables also increased the dataset size beyond that of the aircraft vertical profiles to 4490 samples. The LWP retrieval technique – based on a millimeter wave passive radiometer – was documented in Zuidema et al. (2012), while here we developed a physical algorithm to produce τ from broadband shortwave irradiances collected by an Eppley Precision Spectral Pyranometer. Although similar algorithms, based on pyranometer observations, have been utilized in the past, to our knowledge this is the first time that τ has been retrieved from an airborne pyranometer. We assessed a typical uncertainty in τ of near 10 %, mostly attributed the instrument calibration errors. The remote sensed τ-LWP relationship was consistent with the one derived from the in situ cloud probes. This physical consistency was further supported by the agreement between the parameterized N_d (a function of τ and LWP) and the cloud probe N_d, with a tail of high, physically-unrealistic N_d values consistent with the aggregation of a broader cloud area within the pyranometer flux measurements.

We calculated ACI_τ for different LWP intervals, in order to isolate the effect of the aerosols in the cloud microphysics from other dynamical factors. We found magnitudes of ACI_τ close to the physical upper limit, suggesting that this cloud regime is highly sensitive to changes in the aerosol concentration. Additionally, ACI_τ increased with LWP, and reached a maximum for LWP of 68–70 $g\,m^{-2}$. Scale impacts on ACI, deduced with proxy data in MF12, were apparent in the data analysized here through ACI increases for higher N_d thresholds and with LWP values smoothed using a 15-s running mean.

The albedo relative susceptibility $S_{R-\tau}$ was utilized to study the link between cloud microphysics and radiative response. The analysis indicated that clouds tended to be most susceptible to changes in their albedo for a LWP of 60 $g\,m^{-2}$ and τ of 14, and decreased thereafter. This tendency, especially for $S_{R-\tau}$ and LWP, was in agreement with satellite estimates from MODIS and CERES (Painemal and Minnis, 2012). This is an important result because it demonstrates that despite the coarser spatial resolution and potential retrieval artifacts, satellite observations provide a suitable dataset for estimating the cloud susceptibility in the Southeast Pacific regime. The dissimilar

ACPD
12, 25441–25485, 2012

variation in ACI_{τ} and $S_{R-\tau}$ produced a net first aerosol indirect effect that is a minimum for LWP of 30–40 g m^{-2}, and a maximum for LWP at 68 g m^{-2}, with a modest decrease for larger LWP. These results overall provide further insight and detail on a cloud region, the Southeast Pacific stratocumulus deck, that has the highest cloud radiative response per unit of aerosol perturbation of anywhere on the globe. These 1AIE estimates are also useful for the assessment of large-scale climate model estimates for pristine marine stratocumulus decks.

Acknowledgements. D. Painemal and P. Zuidema were supported by NSF Large-Scale Dynamics Award 0745470 and NSF AGS Award 1233874 (PZ). D. Painemal was also supported by the NASA Postdoctoral Program at the NASA Langley Research Center. The authors are indebted to the staff and instrument scientists of the Research Aviation Facility and the National Center for Atmospheric Research that were involved in the aircraft C-130 operation. Wyoming Cloud Radar and Lidar data set was generously provided by David Leon. Relevant comments from Graham Feingold as a member of D. Painemal's PhD thesis committee are gratefully acknowledged. We also thank Walter Robinson, Robert Wood, Christopher Bretherton, and Roberto Mechoso for their leadership of VOCALS-Rex, making this study possible.

References

Allen, G., Coe, H., Clarke, A., Bretherton, C., Wood, R., Abel, S. J., Barrett, P., Brown, P., George, R., Freitag, S., McNaughton, C., Howell, S., Shank, L., Kapustin, V., Brekhovskikh, V., Kleinman, L., Lee, Y.-N., Springston, S., Toniazzo, T., Krejci, R., Fochesatto, J., Shaw, G., Krecl, P., Brooks, B., McMeeking, G., Bower, K. N., Williams, P. I., Crosier, J., Crawford, I., Connolly, P., Allan, J. D., Covert, D., Bandy, A. R., Russell, L. M., Trembath, J., Bart, M., McQuaid, J. B., Wang, J., and Chand, D.: South East Pacific atmospheric composition and variability sampled along 20° S during VOCALS-REx, Atmos. Chem. Phys., 11, 5237–5262, doi:10.5194/acp-11-5237-2011, 2011.

Bennartz, R.: Global assessment of marine boundary layer cloud droplet number concentration from satellite, J. Geophys. Res., 112, D02201, doi:10.1029/2006JD007547, 2007.

ACPD
12, 25441–25485, 2012

Brenguier, J.-L., Pawlowska, H., Schüller, L., Preusker, R., Fischer, J., and Fouquart, I.: Radiative properties of boundary layer clouds: droplet effective radius versus number concentration, J. Atmos. Sci., 57, 803–821, 2000.

Bretherton, C. S., Wood, R., George, R. C., Leon, D., Allen, G., and Zheng, X.: Southeast Pacific stratocumulus clouds, precipitation and boundary layer structure sampled along 20° S during VOCALS-REx, Atmos. Chem. Phys., 10, 10639–10654, doi:10.5194/acp-10-10639-2010, 2010.

Bush, B. C., Valero, F. P. J, Simpson, A. S., and Bignone, L.: Characterization of thermal effects in pyranometers: a data correction algorithm for improved measurement of surface insolation, J. Atmos. Oceanic Technol., 17, 165–175, 2000.

Cahalan, R. F., Ridgeway, W., Wiscombe, W., Bell, T., and Snider, J. B.: The albedo of fractal stratocumulus clouds, J. Atmos. Sci., 51, 2434–2455, 1994.

Di Girolamo, L., Liang, L., and Platnick S.: A global view of one-dimensional solar radiative transfer through oceanic water clouds, Geophys. Res. Lett., 37, L18809, doi:10.1029/2010GL044094, 2010.

Feingold, G., Remer, L. A., Ramaprasad, J., Kaufman, Y. J.: Analysis of smoke impact on clouds in Brazilian biomass burning regions: an extension of Twomey's approach, J. Geophys. Res., 106, 22907–22922, 2001.

Feingold, G.: Modeling of the first indirect effect: analysis of measurement requirements, Geophys. Res. Lett., 30, 1997, doi:10.1029/2003GL017967, 2003.

Hu Y. X. and Stamnes, K.: An accurate parameterization of the radiative properties of water clouds suitable for use in climate models, J. Climate, 6, 728–742, 1993.

Jones, C. R., Bretherton, C. S., and Leon, D.: Coupled vs. decoupled boundary layers in VOCALS-REx, Atmos. Chem. Phys., 11, 7143–7153, doi:10.5194/acp-11-7143-2011, 2011.

Kato, S., Ackerman, T. P., Clothiaux, E. E., Mather, J. H., Mace, G. G., Wesely, M. L., Murcray, F., and Michalsky, J.: Uncertainties in modeled and measured clear-sky surface shortwave irradiances, J. Geophys. Res., 102, 25881–25898, doi:10.1029/97JD01841, 1997.

Key, J. and Schweiger, A. J.: Tools for atmospheric radiative transfer: streamer and FluxNet, Comput. Geosci., 24, 443–451, 1998.

Leontyeva, E., and Stamnes, K.: Estimations of cloud optical thickness from ground-based measurements of incoming solar radiation in the Arctic, J. Climate, 7, 566–578, 1994.

ACPD
12, 25441–25485, 2012

Kim, B.-G., Miller, M. A., Schwartz, S. E., Liu, Y., and Min, Q.: The role of adiabaticity in the aerosol first indirect effect, J. Geophys. Res., 113, D05210, doi:10.1029/2007JD008961, 2008.
McComiskey, A. and Feingold, G.: Quantifying error in the radiative forcing of the first aerosol indirect effect, Geophys. Res. Lett., 35, L02810, doi:10.1029/2007GL032667, 2008.
McComiskey, A. and Feingold, G.: The scale problem in quantifying aerosol indirect effects, Atmos. Chem. Phys., 12, 1031–1049, doi:10.5194/acp-12-1031-2012, 2012.
McComiskey, A., Feingold, G., Frisch, A. S., Turner, D. D., Miller, M. A., Chiu, J. C., Min, Q., and Ogren, J. A.: An assessment of aerosol-cloud interactions in marine stratus clouds based on surface remote sensing, J. Geophys. Res., 114, D09203, doi:10.1029/2008JD011006, 2009.
Muñoz, R. C. and Garreaud, R.: Dynamics of the low-level jet off the west coast of Subtropical South America, Mon. Weather Rev., 133, 3661–3677, doi:10.1175/MWR3074.1, 2005.
Oreopoulos, L. and Platnick, S.: The radiative susceptibility of cloudy atmospheres to droplet number perturbations: 2. Global analysis from MODIS J. Geophys. Res., 113, D14S21, doi:10.1029/2007JD009655, 2008.
Painemal, D. and Minnis, P.: On the dependence of albedo on cloud microphysics over marine stratocumulus clouds regimes determined from CERES data, J. Geophys. Res., 117, D06203, doi:10.1029/2011JD017120, 2012.
Painemal, D. and Zuidema, P.: Microphysical variability in southeast Pacific Stratocumulus clouds: synoptic conditions and radiative response, Atmos. Chem. Phys., 10, 6255–6269, doi:10.5194/acp-10-6255-2010, 2010.
Painemal, D. and Zuidema, P.: Assessment of MODIS cloud effective radius and optical thickness retrievals over the Southeast Pacific with VOCALS-Rex in-situ measurements, J. Geophys. Res., 116, D24206, doi:10.1029/2011JD016155, 2011.
Pazmany, A.: A compact 183 GHz radiometer for airborne and ground-based water vapor and liquid water sensing, IEEE Trans. Geosci. Rem. Sens., 45, 2202–2206, 2007.
Petty, G. W. (ed.): A First Course in Atmospheric Radiation, Sundog, Madison, WI, 444 pp., 2004.
Pinto, J., Curry, J., and Fairall, C.: Radiative characteristics of the Arctic atmosphere during spring as inferred from ground-based measurements. J. Geophys. Res., 102, 6941–6952, 1997.

ACPD
12, 25441–25485, 2012

Platnick, S. and Oreopoulos, L.: Radiative susceptibility of cloudy atmospheres to droplet number perturbations: 1. Theoretical analysis and examples from MODIS, J. Geophys. Res., 113, D14S20, doi:10.1029/2007JD009654, 2008.

Platnick, S. and Twomey, S.: Determining the susceptibility of cloud albedo to changes in droplet concentration with the advanced very high resolution radiometer, J. Appl. Meteorol., 33, 334–347, 1994.

Ricchiazzi, P., Yang, S., Gautier, S. and Sowle, D.: SBDART: A research and teaching software tool for plane-parallel radiative transfer in the earth's atmosphere, B. Amer. Meteor. Soc., 79, 2101–2114, 1998.

Quaas, J., Ming, Y., Menon, S., Takemura, T., Wang, M., Penner, J. E., Gettelman, A., Lohmann, U., Bellouin, N., Boucher, O., Sayer, A. M., Thomas, G. E., McComiskey, A., Feingold, G., Hoose, C., Kristjánsson, J. E., Liu, X., Balkanski, Y., Donner, L. J., Ginoux, P. A., Stier, P., Grandey, B., Feichter, J., Sednev, I., Bauer, S. E., Koch, D., Grainger, R. G., Kirkevåg, A., Iversen, T., Seland, Ø., Easter, R., Ghan, S. J., Rasch, P. J., Morrison, H., Lamarque, J.-F., Iacono, M. J., Kinne, S., and Schulz, M.: Aerosol indirect effects – general circulation model intercomparison and evaluation with satellite data, Atmos. Chem. Phys., 9, 8697–8717, doi:10.5194/acp-9-8697-2009, 2009.

Street, J. O., Carroll, R. J., and Ruppert, D.: A note on computing robust regression estimates via iteratively reweighted least squares, Am. Stat., 42, 152–154, doi:10.2307/2684491, 1988.

Twohy, C. H., Petters, M. D. Snider, J. R., Stevens, B., Tahnk, W., Wetzel, M., Russell, L., and Burnet, F.: Evaluation of the aerosol indirect effect in marine stratocumulus clouds: droplet number, size, liquid water path, and radiative impact, J. Geophys. Res., 110, D08203, doi:10.1029/2004JD005116, 2005.

Twomey, S.: The influence of pollution on the short wave albedo of clouds, J. Atmos. Sci., 34, 1149–1152, 1977.

Wood, R., Mechoso, C. R., Bretherton, C. S., Weller, R. A., Huebert, B., Straneo, F., Albrecht, B. A., Coe, H., Allen, G., Vaughan, G., Daum, P., Fairall, C., Chand, D., Gallardo Klenner, L., Garreaud, R., Grados, C., Covert, D. S., Bates, T. S., Krejci, R., Russell, L. M., de Szoeke, S., Brewer, A., Yuter, S. E., Springston, S. R., Chaigneau, A., Toniazzo, T., Minnis, P., Palikonda, R., Abel, S. J., Brown, W. O. J., Williams, S., Fochesatto, J., Brioude, J., and Bower, K. N.: The VAMOS Ocean-Cloud-Atmosphere-Land Study Regional Experiment (VOCALS-REx): goals, platforms, and field operations, Atmos. Chem. Phys., 11, 627–654, doi:10.5194/acp-11-627-2011, 2011.

ACPD
12, 25441–25485, 2012

Yang, Q., W. I. Gustafson Jr., Fast, J. D., Wang, H., Easter, R. C., Morrison, H., Lee, Y.-N., Chapman, E. G., Spak, S. N., and Mena-Carrasco, M. A.: Assessing regional scale predictions of aerosols, marine stratocumulus, and their interactions during VOCALS-REx using WRF-Chem, Atmos. Chem. Phys., 11, 11951–11975, doi:10.5194/acp-11-11951-2011, 2011.

Zhang, Z. and Platnick, S.: An assessment of differences between cloud effective particle radius retrievals for marine water clouds from three MODIS spectral bands, J. Geophys. Res., 116, D20215, doi:10.1029/2011JD016216, 2011.

Zheng, X., Albrecht, B., Jonsson, H. H., Khelif, D., Feingold, G., Minnis, P., Ayers, K., Chuang, P., Donaher, S., Rossiter, D., Ghate, V., Ruiz-Plancarte, J., and Sun-Mack, S.: Observations of the boundary layer, cloud, and aerosol variability in the southeast Pacific near-coastal marine stratocumulus during VOCALS-REx, Atmos. Chem. Phys., 11, 9943–9959, doi:10.5194/acp-11-9943-2011, 2011.

Zuidema, P. and Evans, K. F.: On the validity of the independent pixel approximation for boundary layer clouds observed during ASTEX, J. Geophys. Res., 103, 6059–6074, 1998.

Zuidema, P., Baker, P., Han, Y., Intrieri, J., Key, J., Lawson, P., Matrosov, S., Shupe, M., Stone, R., and Uttal, T.: An Arctic springtime mixed-phase cloudy boundary layer observed during SHEBA, J. Atmos. Sci., 62, 160–176, 2005.

Zuidema, P., Painemal, D., de Szoeke, S., and Fairall, C.: Stratocumulus cloud top height estimates and their climatic implications, J. Climate, 22, 4652–4666, 2009.

Zuidema, P., Leon, D., Pazmany, A., and Cadeddu, M.: Aircraft millimeter-wave passive sensing of cloud liquid water and water vapor during VOCALS-REx, Atmos. Chem. Phys., 12, 355–369, doi:10.5194/acp-12-355-2012, 2012.

ACPD
12, 25441–25485, 2012

Table 1. C-130 research flights and periods analyzed in this study. Local time is approximately UTC-5.

Name	2008 Date	Time (UTC)
Research Flight 01 (RF01)	15 Oct	17:47–19:27
Research Flight 02 (RF02)	18 Oct	13:46–19:10
Research Flight 11 (RF11)	9 Nov	13:42–20:12
Research Flight 12 (RF12)	11 Nov	14:23–20:55

ACPD
12, 25441–25485, 2012

Table 2. Regression values used to correct the pyranometer irradiance $Q_{\text{pyr-adj}} = aQ_{\text{pyr}} + b$.

	a	B (W m^{-2})
RF01	0.97	25
RF02	0.92	12
RF11	0.9	68
RF12	0.91	41

ACPD
12, 25441–25485, 2012

Table 3. Variables and instrument dependences.

Measurements	Instruments
LWP	ProSensing G-band radiometer
τ	Eppley Precision Spectral Pyranometer
Aerosols, N_a	DMT's Passive Cavity Aerosol Spectrometer Probe (PCASP), sizes: [0.1 µm 3.0 µm]
Reflectivity/cloud base height	University of Wyoming W-band Radar/Lidar
N_d	$f(\mathrm{LWP}, \tau)$

ACPD
12, 25441–25485, 2012

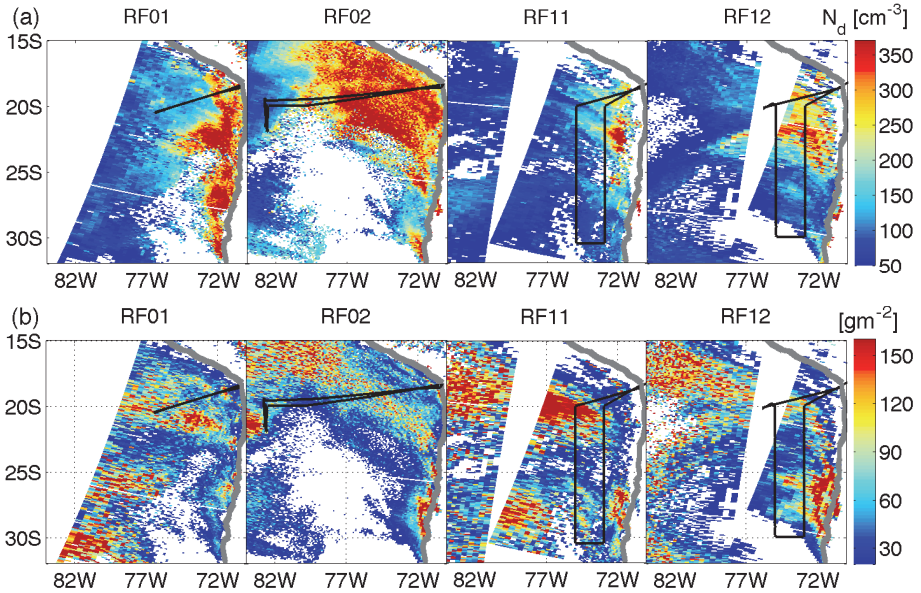

Fig. 1. MODIS-Terra maps for each research flight. **(a)** N_d and **(b)** LWP. The black solid lines indicate the aircraft track. The thick gray line represents the coastal line.

ACPD
12, 25441–25485, 2012

The first aerosol indirect effect

D. Painemal and P. Zuidema

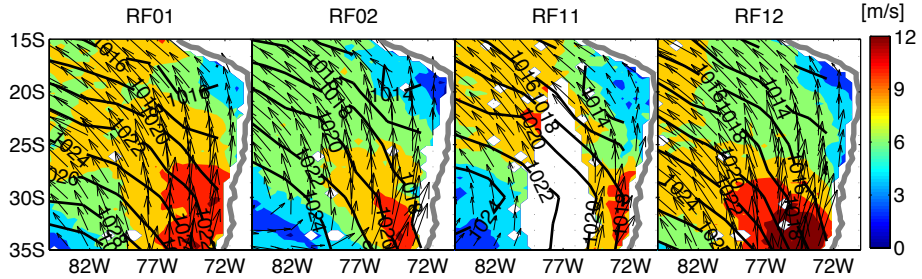

Fig. 2. Daily mean wind direction (arrows) and magnitude (colors) from NASA's Quick Scatterometer (QuikScat). The black contours are the reanalyzed daily sea level pressure from the NCEP/NCAR.

ACPD
12, 25441–25485, 2012

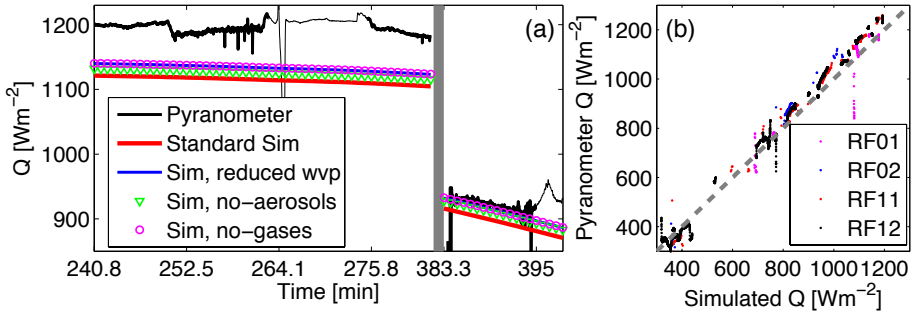

Fig. 3. Simulated and pyranometer irradiances: **(a)** time series during RF12. The pyranometer irradiance is denoted by the black line, and the thick black line represents periods with clear-sky conditions. The red line is the standard simulation, whereas the blue line, green triangles, and magenta circles represent the simulations with 50 % reduction in water vapor, pristine conditions, and negligible absorbing gases, respectively. **(b)** Scatterplot between the pyranometer irradiance and the simulated one for above-clouds observations.

ACPD
12, 25441–25485, 2012

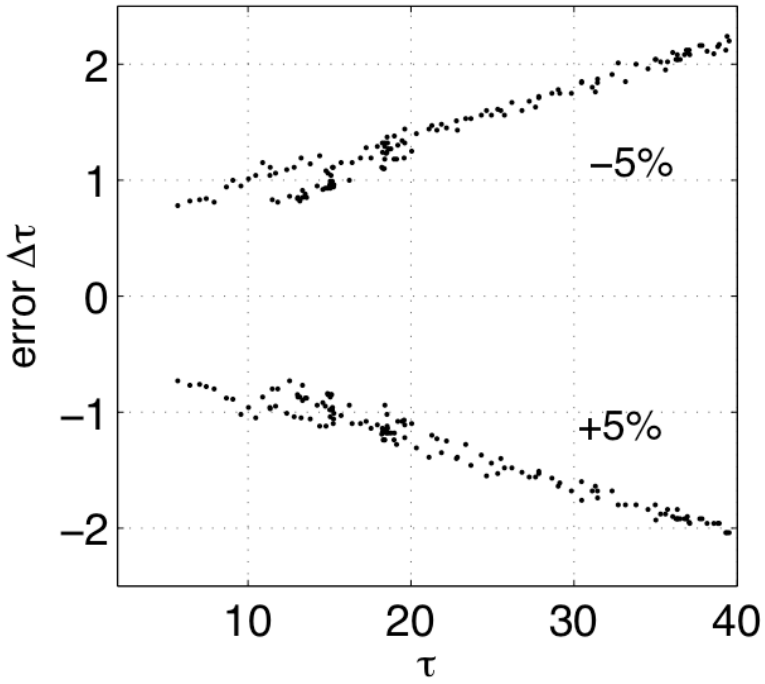

Fig. 4. Error in τ associated with a 5 % uncertainty in the pyranometer measurements.

ACPD
12, 25441–25485, 2012

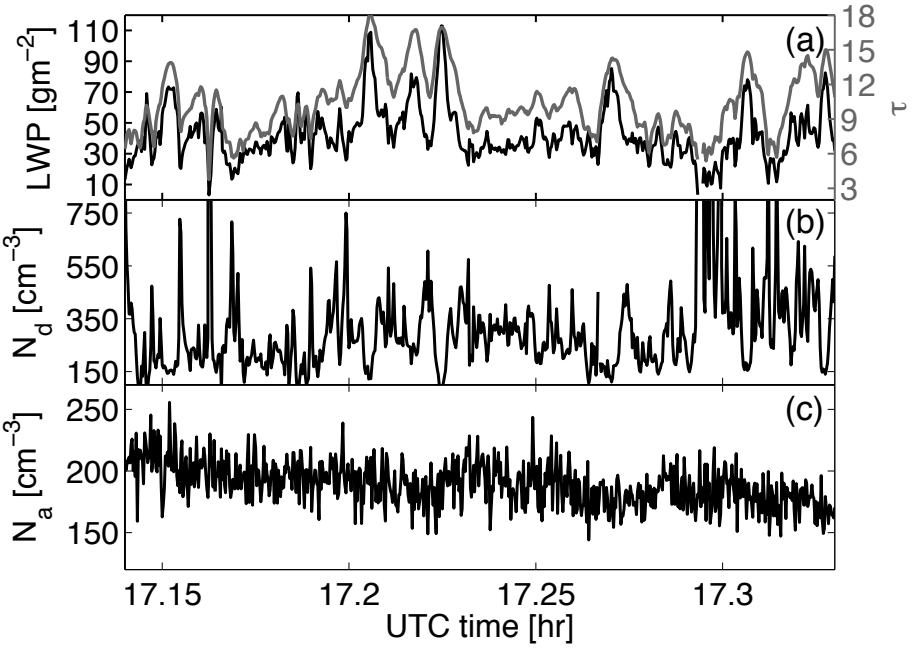

Fig. 5. Example of time series during 18 October research flight (RF02): **(a)** GVR LWP (black) and τ (gray), **(b)** N_d from Eq. (8), **(c)** accumulation mode aerosol concentration N_a.

ACPD
12, 25441–25485, 2012

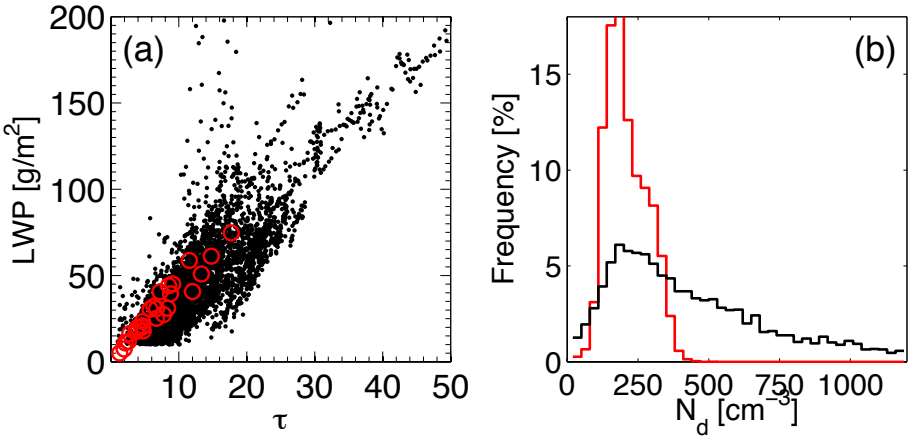

Fig. 6. (a) LWP versus τ. Black dots represent the remote sensed values, and the red circles are the values derived from the cloud probes. **(b)** Histograms for the remote sensing-based N_d (black line) and the in-situ N_d obtained during in-cloud legs (red line).

ACPD
12, 25441–25485, 2012

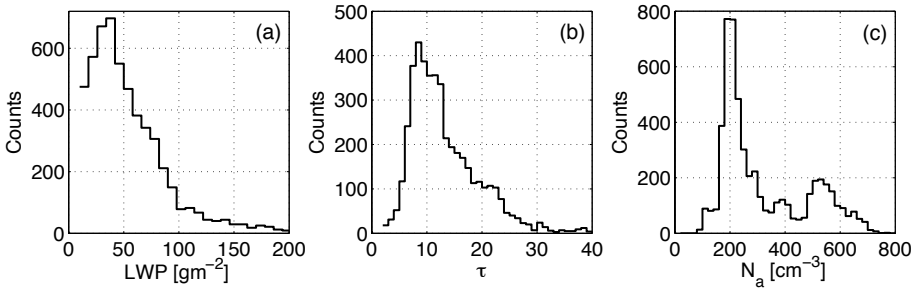

Fig. 7. Histograms for **(a)** LWP, **(b)** τ, and **(c)** N_a.

ACPD
12, 25441–25485, 2012

The first aerosol indirect effect

D. Painemal and P. Zuidema

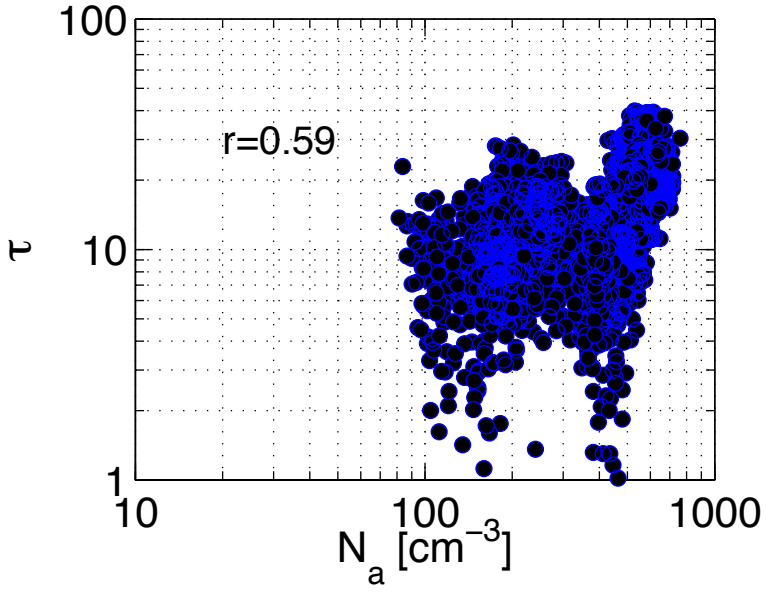

Fig. 8. Scatterplot between N_a and τ.

ACPD
12, 25441–25485, 2012

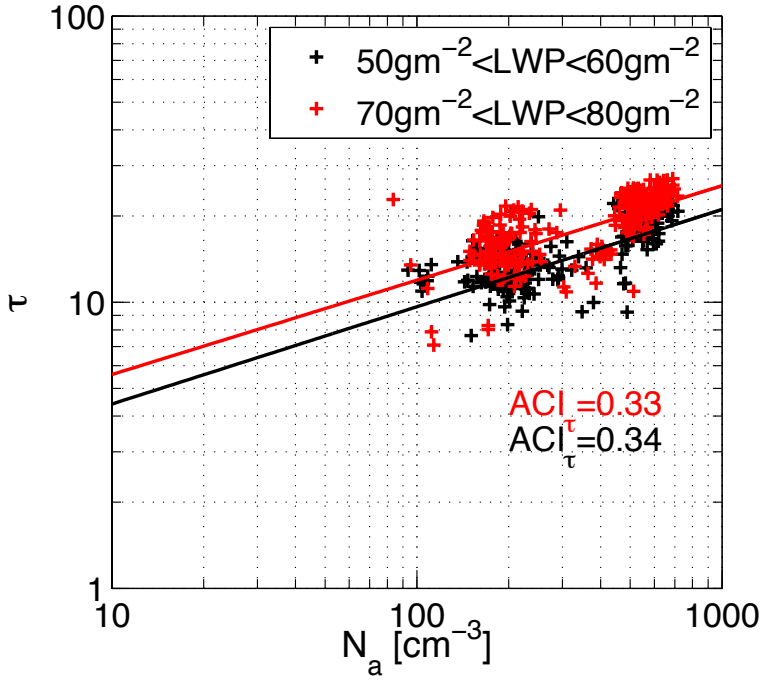

Fig. 9. Scatterplot between N_a and τ. Solid lines are the linear fit for each LWP bin.

ACPD
12, 25441–25485, 2012

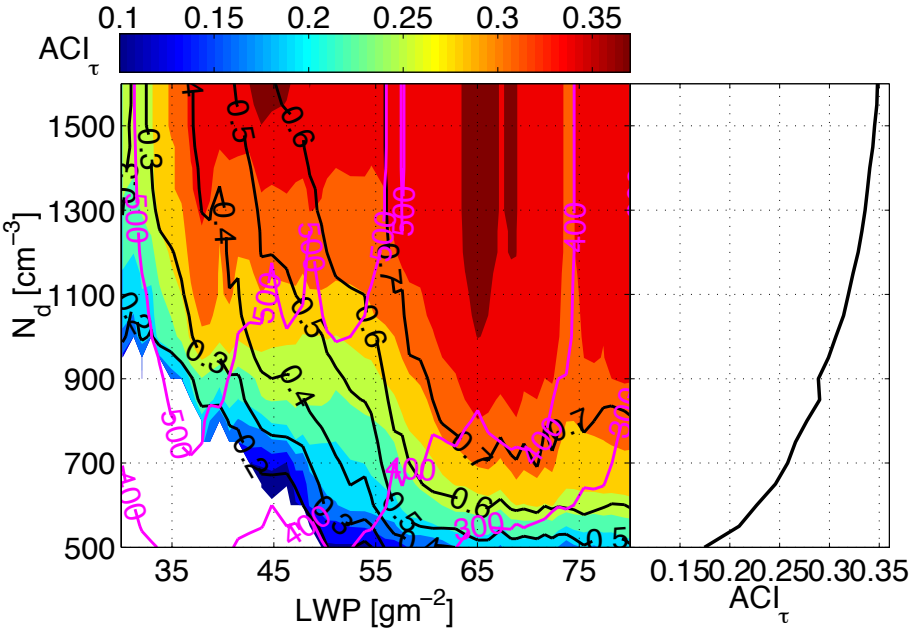

Fig. 10. ACI$_\tau$ as a function of LWP and for different upper N_d thresholds (left panel). Black and magenta contours indicate the linear correlation and number of samples per bin, respectively. ACI$_\tau$ and correlations are statistically significant at the 99.9 % confidence level according to a one-tailed Student's t test. The right panel corresponds to the average ACI$_\tau$ per N_d threshold.

ACPD
12, 25441–25485, 2012

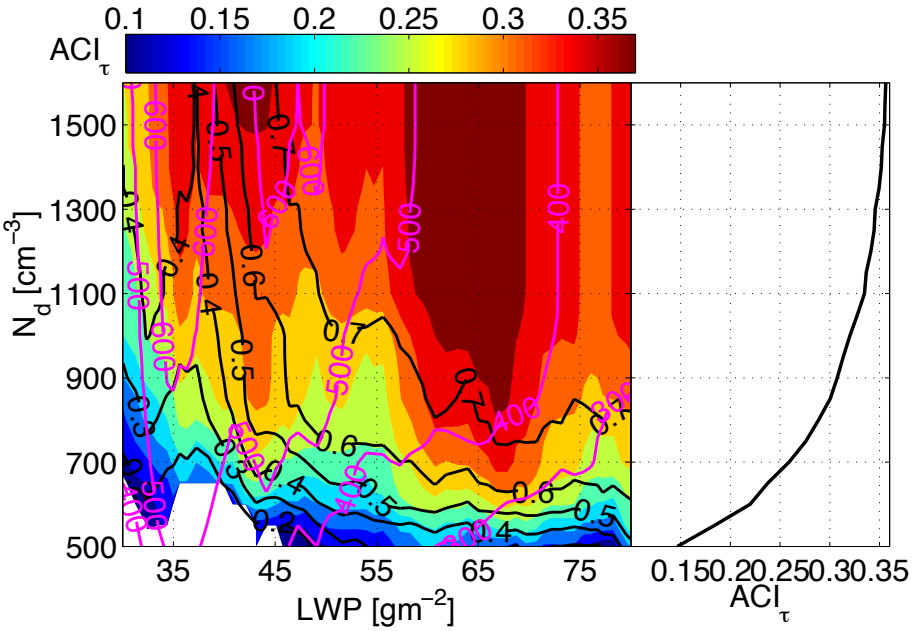

Fig. 11. As in Fig. 10, but for a 15-s LWP running mean.

ACPD
12, 25441–25485, 2012

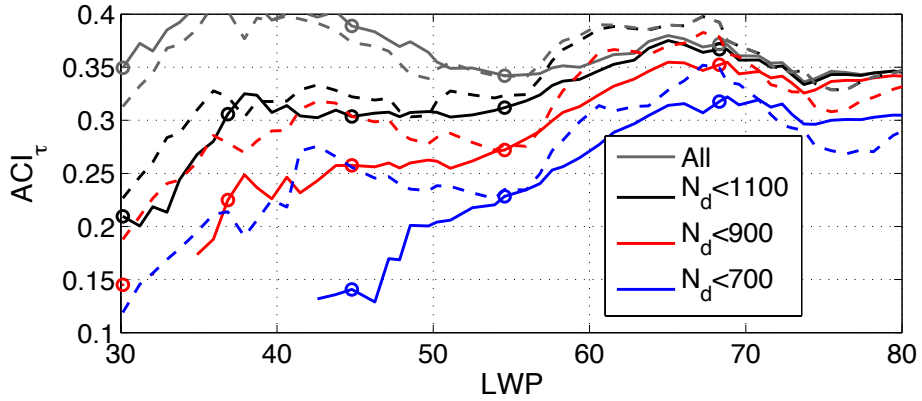

Fig. 12. ACI$_\tau$ as a function of LWP bins. Cases with N_d smaller than 1100, 900, and 700 cm^{-3} are denoted by black, red, and blue lines, respectively. Dashed lines indicate ACI$_\tau$ calculated with a 15-s running mean LWP and N_a. Values are statistically significant according to a Student's t test at the 99 % confidence level. Circles indicate bins without overlapping.

ACPD
12, 25441–25485, 2012

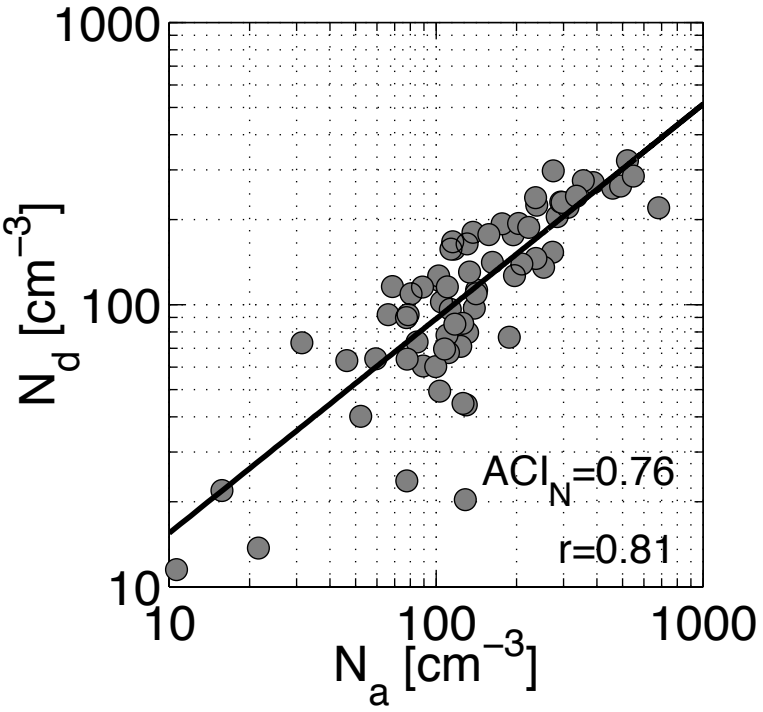

Fig. 13. Scatterplot between N_a and in situ N_d.

ACPD
12, 25441–25485, 2012

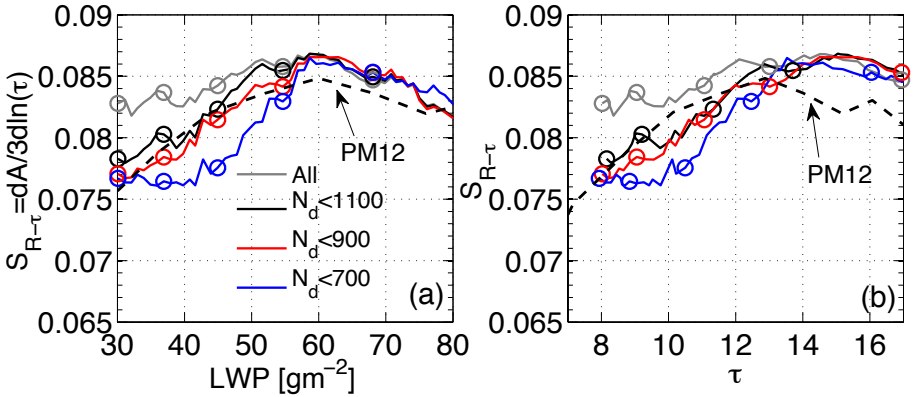

Fig. 14. Albedo relative susceptibility as a function of **(a)** LWP and **(b)** τ (binned as a function of LWP). Gray, black, red, and blue lines correspond to calculation made with all the data, $N_d < 1100$, $N_d < 900$, and $N_d < 700\,\mathrm{cm}^{-3}$, respectively. Black dashed lines (PM_{12}) are relative susceptibilities reported in Painemal and Minnis (2012) over the Southeast Pacific near the coast. Circles indicate bins without overlapping.

ACPD
12, 25441–25485, 2012

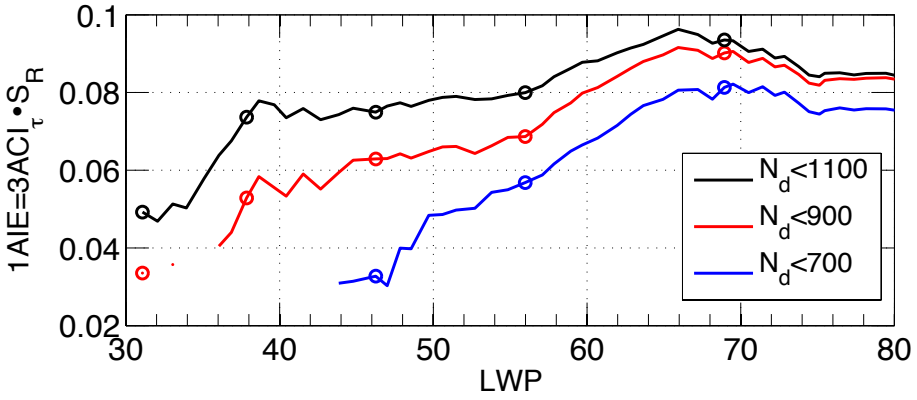

Fig. 15. The first aerosol indirect effect expressed as 1AIE = 3ACI$_\tau S_{R-\tau}$. Colors and symbols are defined in Figs. 12 and 14.

ACPD
12, 25441–25485, 2012